PCCP

Physical Chemistry Chemical Physics

rsc.li/pccp

25 YEARS
ANNIVERSARY

ROYAL SOCIETY
OF **CHEMISTRY**

PAPER
Y. Stergiou, K. Schwarzenberger *et al.*
Flow-driven pattern formation during coacervation of
xanthan gum with a cationic surfactant

PCCP
Owner Societies

PAPER

Check for updates

Flow-driven pattern formation during coacervation of xanthan gum with a cationic surfactant†

Y. Stergiou, [ID] ⋆[ab] A. Perrakis, [ID] [ab] A. De Wit [ID] [c] and K. Schwarzenberger [ID] ⋆[ab]

We experimentally demonstrate that the coacervation of a biopolymer can trigger a hydrodynamic instability when a coacervate is formed upon injection of a xanthan gum dispersion into a cationic surfactant ($C_{14}TAB$) solution. The local increase of the viscosity due to the coacervate formation induces a viscous fingering instability. Three characteristic displacement regimes were observed: a viscous fingering dominated regime, a buoyancy-controlled "volcano" regime and a "fan"-like regime determined by the coacervate membrane dynamics. The dependence of the spatial properties of the viscous fingering pattern on the Péclet and Rayleigh numbers is investigated.

1 Introduction

Complex coacervation is the separation of a macromolecular solution, *e.g.* a polymer solution, into a dense polymer-rich coacervate phase and a polymer-lean equilibrium phase by interaction with an oppositely-charged molecular species.[1] The biopolymer xanthan gum (XG) forms coacervates when mixed with cationic surfactants like tetradecyltrimethylammonium bromide ($C_{14}TAB$).[2] By this process, functional capsules[3,4] and membrane layers at the interface between the polymer–surfactant solution[5] or at the air–solution interface[6] can be obtained in a self-assembly process.[7] The mechanical properties of these functional materials can be easily tuned, *e.g.*, by varying the preparation conditions and the solution concentrations.[5,8] XG derived gels have recently been suggested for bioremediation or cell immobilization purposes[9] as well as applications in porous media (*i.e.* functional layer formation in soils[10]).

For such applications, the reactant solutions are typically injected radially into the porous medium. In that case, if a less viscous fluid displaces a more viscous one in confined geometries, such as geological pores, packed beds or Hele–Shaw (HS) cells, the interface (immiscible) or the contact zone (miscible) becomes unstable producing a fingerlike pattern, due to a viscous fingering (VF) instability.[11] In the reverse stable displacement of a less viscous solution by a more viscous one, chemical reactions can induce hydrodynamic fingering instabilities by triggering non-monotonic viscosity profiles.[12–15] Reactive VF phenomena are ubiquitous in cutting-edge technological applications such as in CO_2 sequestration,[16] thin-film applications,[17] Li-ion batteries design[18] or even in cases related to biofilm generation.[19]

Reaction-driven VF can typically occur when the product of the reaction induces a local maximum in viscosity, creating locally a positive viscosity gradient in the flow direction which in turn results in a hydrodynamic instability that leads to finger growth.[12] There are numerous studies investigating chemically triggered fingering instabilities, *e.g.*, in systems with precipitation,[20–22] pH-sensitive polymers,[13,23,24] and reactive micellar fluids.[25]

Also flow displacements in gel systems[26,27] or in systems involving physico-chemical processes such as phase separation,[28,29] spinodal decomposition[30] and viscoelastic effects[31] produce a variety of displacement patterns. Due to the altered rheological properties during complex coacervation,[2] fingering effects may also be expected in such systems. As a result of the hydrodynamic instability, the spatiotemporal distribution of the coacervate phase is drastically altered. This effect was not characterized until now, but is highly relevant for the mentioned applications.

Motivated by the above, we show that a novel landscape of reaction-driven VF dynamics emerges when injecting a more viscous XG solution into a less viscous solution of the cationic surfactant $C_{14}TAB$ (Fig. 1(a)). An instability is triggered by the coacervation process through a synergy of phase transition, interfacial phenomena and complex rheology of the formed coacervate.[2] The coacervation process is initiated upon contact

a Institute of Fluid Dynamics, Helmholtz-Zentrum Dresden-Rossendorf, Bautzner Landstr. 400, 01328 Dresden, Germany. E-mail: g.stergiou@hzdr.de, k.schwarzenberger@hzdr.de

b Institute of Process Engineering and Environmental Technology, Technische Universität Dresden, 01062 Dresden, Germany

c Nonlinear Physical Chemistry Unit, Service de Chimie Physique et Biologie Théorique, Faculté des Sciences, Université Libre de Bruxelles (ULB), CP 231, 1050 Brussels, Belgium

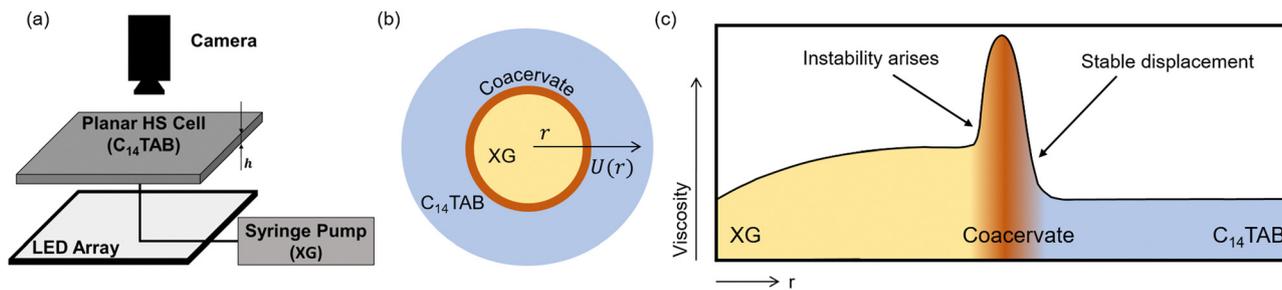† Electronic supplementary information (ESI) available: List of the experimental parameters, details on the temporal pattern evolution. See DOI: https://doi.org/10.1039/d4cp01055h

Fig. 1 Sketch of the experimental system used: (a) the Hele–Shaw cell is initially filled with the $C_{14}TAB$ solution, the XG dispersion is then injected through the center of the Hele–Shaw cell at a constant flow rate. (b) By the injection, the coacervate (product) spreads radially in the Hele–Shaw cell. (c) Schematic sketching of the radial viscosity change.

between the aqueous dispersion of the XG macromolecule[32,33] and the surfactant solution.[5] With increasing surfactant concentration, the polymer is progressively covered with surfactant molecules.[34] In this way, polymer–surfactant and polymer–micelle complexes are formed which consume the free surfactant molecules and micelles. If concentration gradients are present, as in our radial injection system, kinetically trapped states of the polymer–surfactant complexes can also form, which deviate from the equilibrium situation in an ideally mixed system. During these processes, the negatively charged sites along the XG chains[35] are partly neutralized by positively charged $C_{14}TAB$ molecules. This induces a phase separation of the formed hydrophobic XG-$C_{14}TAB$ complexes into a dense coacervate and a polymer-lean phase.[36] The local production of the coacervate phase ("weak gel") introduces locally a maximum in the viscosity profile in the vicinity of the contact line between the two fluids, *cf.* Fig. 1(b) and (c). This causes a local streamwise positive gradient of viscosity, which in turn favours VF.

2 Experimental

We used a horizontally placed Hele–Shaw (HS) cell, *i.e.* a thin fluid gap between two plexiglass plates as shown in Fig. 1, with different gap height values (h) of 0.1, 0.25, 0.5, 0.6 and 0.75 mm. The HS cell was initially filled with a solution of $C_{14}TAB$ (98% purity, Sigma-Aldrich), a cationic surfactant, at 4.04 g l^{-1} (a concentration 3 times the critical micelle concentration). The viscosity of the $C_{14}TAB$ solution is $\mu_1 = 0.976$ mPa s and the density $\rho_1 = 0.9793$ g ml^{-1}. The displacing XG (Sigma-Aldrich) dispersion was injected through a centrally placed inlet. XG is an anionic polysaccharide with known shear-thinning properties, such that the viscosity depends on the radial distance r from the injection point in the region with XG, as depicted in Fig. 1(c). For high shear rates, the viscosity of the XG dispersion can be derived from the literature[37] as $\mu_2 = 5.1$ mPa s at the used concentration of 3 g l^{-1}. The dispersion was injected with a constant flow rate, q, ranging from 0.005 to 5 ml min^{-1}, with the use of a syringe pump (PHD ULTRA, Harvard Apparatus, Holliston, MA, USA) and a syringe (Hamilton Company, Reno, NV, USA). For the preparation of the XG dispersion, to ensure maximum dispersity, the solution was

stirred for 40 minutes at 13 000 rpm using an Ultra-Turrax T25 rotor-stator homogenizer (IKA-Werke, Staufen, Germany). The density of the 3 g l^{-1} XG dispersion is $\rho_2 = 1.0023$ g ml^{-1}.

The density values and the $C_{14}TAB$ solution viscosity were measured at 25 °C, using an SVM 3001 pycnometer-viscosimeter (Anton Paar GmbH, Graz, Austria). The instability was visualized using traces of Fuchsine dye (0.4 g l^{-1}) added to the XG dispersion. A camera (GO-5100M, JAI A/S, Copenhagen, Denmark) was mounted to take images from a top view, along with an LED array (Smart Vision Lights, Norton Shores, MI, U.S.A.) to illuminate from the bottom. Fuchsine was added to enhance the visual observations, but did not affect the behavior of the displacements, as cross-checked by comparing runs with and without the dye.

To analyze the dynamics, we made use of two non-dimensional quantities, namely, the Péclet number, Pe = $q/2\pi hD$, as defined in the literature[38] for similar systems, and a solutal Rayleigh number, Ra = $(\rho_2 - \rho_1)h^3g/\mu D$ to account for buoyancy effects. Here, D is a diffusion coefficient set equal to 10^{-10} m^2 s^{-1}, as a relative order of magnitude, because different species with different D are involved,[33,39] coupled with ion effects.[40] For the viscosity value in Ra, an averaged representative viscosity $\mu = (\mu_1 + \mu_2)/2$ has been used. As the chemical system is not altered in our experiments, the Pe number is used to indicate the relative intensity of advective and diffusive phenomena, only controlled by q and h.

The spatio-temporal density distribution of the fluid in the Hele–Shaw gap is more complex than the simple density difference between the displaced and displacing solution ($\rho_2 - \rho_1$) used in Ra. The XG is gradually covered with surfactant, until it becomes hydrophobic enough to phase-separate by coacervation. The polymer and surfactant solution within the coacervation zone are depleted with respect to the corresponding bulk solutions. The formed coacervate is denser than the surrounding surfactant solution.[34] These effects can influence the detailed pattern evolution. The different contributions to the spatio-temporal density distribution (the increasing coverage of the polymer with surfactant, the coacervate phase, and the depleted solutions with different concentrations resulting from the ongoing mass transfer and coacervation) cannot be quantified by a single parameter. At larger distances from the coacervation zone, the densities still correspond to those of the original bulk solutions, which mix with the

depleted regions by diffusion and buoyant convection because of the horizontal density gradients. Hence, for simplicity, the Ra number for an overall description of the system is based on the original solution densities ($\rho_2 - \rho_1$). The Ra number is tuned in the experiments by varying the gap height, h. The detailed values of the experimental parameters are listed in the ESI.†

3 Results and discussion

Fig. 2 depicts the resulting unstable displacements for different Ra and Pe. Three distinct displacement flow regimes emerge: an inwards Viscous Fingering regime (VF), a ''fan''-like regime and a buoyancy-dominated ''volcano'' regime. All of them result from the coacervation process occurring between the XG dispersion and the $C_{14}TAB$ solution with the creation of a separate coacervate polymer-rich phase. They are, therefore, absent when one of the reactants is missing.

As underlying mechanism for the VF cases similar to Fig. 2(a), a local maximum in viscosity is induced by the creation of the coacervate phase and a backward fingering pattern is observed where the fingering pattern develops from the front tip towards the injection point. The high injection velocities in the VF regime provide less time for the coacervation and cause a strongly stretched coacervation zone. This prevents the formation of a dense, membrane-like layer separating both solutions. The fingers are conserved throughout the whole experiment duration and radially arrange with a certain spatial periodicity, reminiscent of the backward reactive VF observed by Riolfo et al.[13]

For higher Ra numbers (and moderate to high Pe), as shown in Fig. 2(b), coarser finger structures are obtained. They are in the mm to cm range for the fan regime, while being in the sub-mm range for the fine viscous fingering pattern. In addition, the outer perimeter of the displacement starts showing signs of a symmetry breaking. This generates a regime that shares similarities with the ''fan''-like structures observed by Podgorski et al.[25] as well as with biofilm growth patterns.[19] In these large Ra cases obtained for higher gap height, h, the shear rate of the flow is significantly reduced, so that the injected XG solution is less stretched and a denser coacervate material can be formed compared to the VF cases. However, as visible from Fig. 2(b), no complete membrane surrounds the injection pattern yet in the ''fan'''-like regime. Nevertheless, the denser coacervate results in an increased effect of its mechanical (i.e. viscoelastic) properties on the overall displacement flow. It has been reported that yield stress materials can significantly alter the fingering pattern characteristics, such as the finger wavelength and compactness,[41–43] and introduce a transition from yield stress dominated to viscous behavior. The membrane still covers the full gap height of the HS cell and probably experiences complex wall interactions (e.g. slip effects[44]) that affect the total flow. In this synergistic regime, viscous fingers are still visible growing inwards, but interact with a pronounced bulging of the viscoelastic material. Nevertheless, no buoyancy effects are observed yet, as the advective flow still dominates the dynamics of the displacement. These processes in the ''fan'' regime appear as distinct features of the developing injection pattern (cf. Fig. S1 and S2 in the ESI†). The areas of dense coacervate are radially displaced by the injected flow and bulge at the same time. The bulging makes the pattern asymmetrical. The absence of pronounced buoyancy effects yields a coacervate zone which spans across the gap width of the HS cell and advances as a front in the radial direction. Fig. S1 and S2 (ESI†) visualize the underlying dynamics where the coacervate pattern grows steadily (in contrast to the volcano regime), but at the same time loses the radial symmetry of the fingering regime (no circular pattern outline).

For displacements where the Ra number is high enough and Pe is low, a buoyancy-induced layering of the coacervate dominates over forced advection, thus a different pattern emerges (cf. Fig. 2(c)). The denser XG solution creeps underneath the surfactant solution, while the coacervate membrane forms, leading to a layered pattern that spreads outwards without any radial symmetry. In the non-reactive case, when injecting the XG dispersion into pure water, a slight buoyancy-driven instability can also emerge for large gap widths (cf. ESI,† Fig. S3) due to the density difference between both fluids as
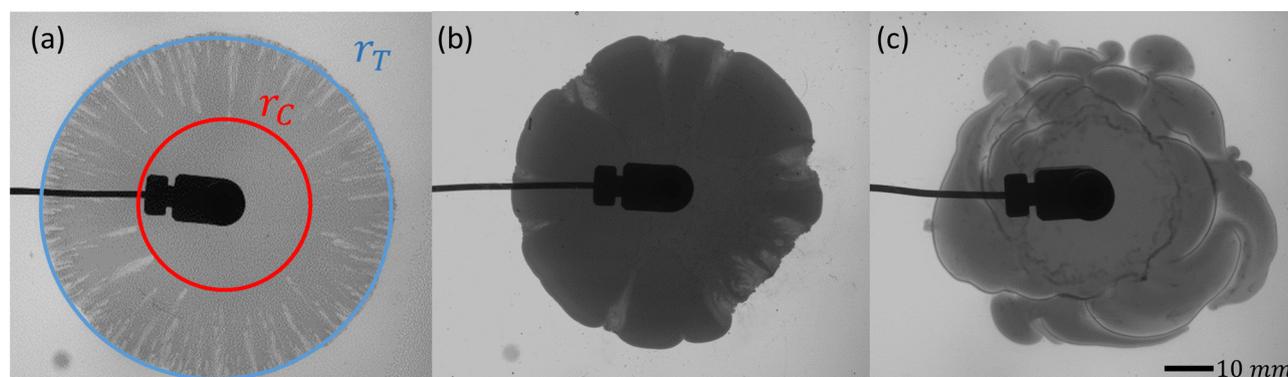

Fig. 2 Different instability regimes of the displacement of a $C_{14}TAB$ solution by a XG dispersion under steady flow rate: (a) viscous fingering, Pe = 106 099 and Ra = 876, the two characteristic radii of the instability are also shown (r_C and r_T); (b) ''fan'' regime, Pe = 13 262 and Ra = 189 292 and (c) ''volcano'' regime, Pe = 3537 and Ra = 369 711.

2922 | Phys. Chem. Chem. Phys., 2025, **27**, 2920–2926

This journal is © the Owner Societies 2025

also observed in previous experiments.[45–47] However, this simpler type of instability clearly differs from the synergistic coacervation- and buoyancy-driven pattern formation in the volcano regime. In Fig. 2(c), a case with such a layered coacervate pattern is shown. The 3D growth of the pattern is confirmed in Fig. S2 in the ESI† by analyzing the temporal change of the area of the pattern as proposed in the work of Wagatsuma and Higashi.[48] The highly asymmetric bulging results from the fact that the injected solution ruptures the formed gel-like membrane in different places. The injected XG dispersion then flows through the membrane gaps and continues to feed the coacervation process, hence new membrane material is created. As in these cases, the buoyancy effects combine with the coacervate formation, the patterns resemble viscous gravity-driven flows with solidifying crust,[49] appearing in lava flows which cool down from the surface. Hence, we coin this pattern as the "volcano" regime, where the membrane formation takes the role of the solidifying crust. This shows that different types of phase transitions can induce similar types of flow patterns, triggered by density differences. In Fig. 2(c), the backward VF mechanism was absent from the beginning; the mechanism responsible for the pattern formation is the buoyancy-driven gravity current and the phase change itself.

Having identified the characteristic pattern types and the main underlying instability mechanisms, we are able to construct a Ra–Pe flow map as shown in Fig. 3. The pattern types are classified into the three regimes at a time t when the individual pattern filled a radius of 2.5 cm from the injection point. Ra and Pe are varied by changing the gap height, h, and flow rate, q (see ESI†). The advection by the injection flow (increasing with increasing Pe) leads both to shearing of the contact zone between the two solutions and to the radial spreading, while triggering the viscous fingering instability. The flow conditions also have a direct effect on the rheological properties and on the mechanical response of the coacervate zone. The reciprocal of Pe further characterizes the kinetics of the membrane formation, as the membrane has more time to grow for smaller Pe. On the other hand, Ra quantifies the increasing influence of buoyancy with increasing h while the shear rate is inversely proportional to h.

The description of this complex system with the two parameters Pe and Ra is a strong simplification, as various mechanisms take place during the displacement. Nevertheless, the map in Fig. 3 allows us to identify which conditions favour a certain pattern, and to better understand the interrelations between the underlying mechanisms. We can observe that, as the influence of advection increases (higher Pe), there are cases where the pattern can transition from the gravity-dominated "volcano" pattern to a VF pattern, passing through the "fan" zone. The "volcano" regime requires small Pe numbers, otherwise advection dominates over the slow velocities of the buoyancy convection for thin vertical length scales. Under small Pe conditions, the time scale is also large enough and the shear forces are low enough to enable the coacervate membrane to form and re-heal after rupture. If the shear rate is too high (small Ra and high Pe), the contact zone between both solutions is strongly stretched and no compact, localized membrane can develop. In that case, only a VF pattern is obtained.

Generally, fingering instabilities are present in all regimes due to the coacervation in the contact zone (a viscosity increase is induced in every case) if the flow velocity exceeds a threshold below which disturbances are dampened by dissipative effects. However, a pronounced membrane formation and its complex rheology causes the change from VF to bulging ("fan" regime) due to the viscoelastic properties of the coacervate. The time during which a membrane can form is similar for constant Pe numbers, as the developing patterns are sampled at the same displacement radius for the regime map. Smaller gaps however increase the shear rate which limits the "fan" and "volcano" regimes to the higher Ra magnitudes.

Due to the radially decaying flow velocities (with increasing distance from the injection point), a time-dependent pattern transition may additionally occur.[50] If the buoyancy-driven "volcano" regime is observed from the beginning, no temporal change to another regime will take place, as it appears for low flow velocities which further diminish as the displacement moves towards the outer regions (higher r). For a VF pattern however, after enough time, when the displacement reaches towards the outer areas of the HS cell, the influence of advection and shear decreases. In that case, because of the radial decay of the local flow velocity, buoyancy effects start to dominate and a layered pattern can start to form. During this process, the initially formed VF pattern shrinks, and as the time scales are large enough, it starts healing due to diffusive mass transfer and additional coacervate formation, as shown in Fig. 4. It is also expected that, given enough time, the VF pattern will ultimately heal into a continuous membrane in all cases, because of the continuous supply of reactants by diffusive mass transfer.

To quantify the VF pattern, we compute the area ratio, d_{α}:

$$d_{\alpha} = \frac{A_{C}}{A_{T}} = \frac{r_{C}^2}{r_{T}^2}, \tag{1}$$
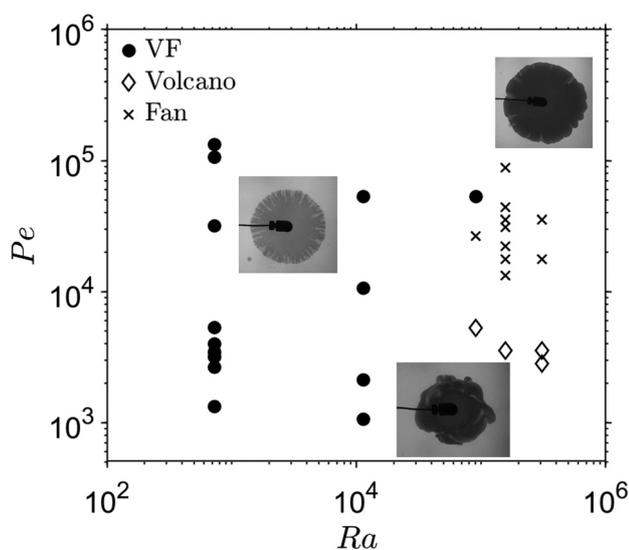

Fig. 3 Flow regime map of the displacement in the Pe–Ra phase space. Three different regimes are identified: the viscous fingering regime (VF); the "fan" regime and the "volcano" regime.
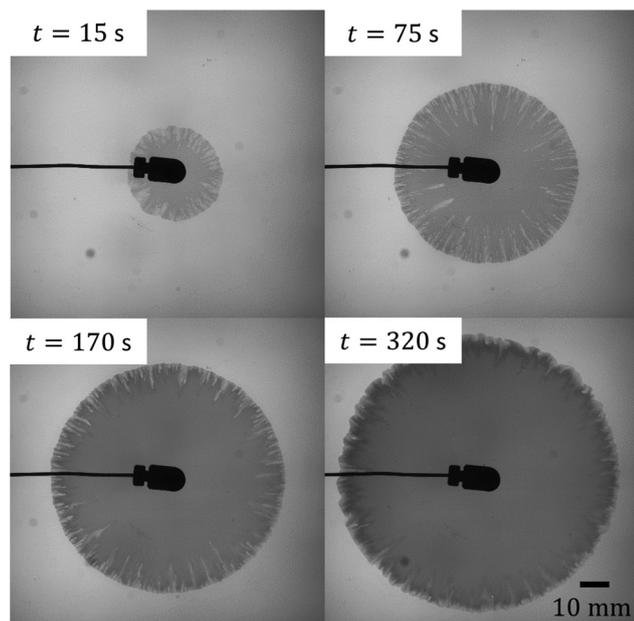
This journal is © the Owner Societies 2025

Phys. Chem. Chem. Phys., 2025, **27**, 2920–2926 | **2923**

Fig. 4 Time progression of VF instability (Pe = 106 099 and Ra = 876). As the instability interface moves towards the rim, the membrane and buoyancy contribution is intensified as a result of the radial velocity decay. The fingers start to heal but the initial VF effect on the membrane remains visible.

where A_T is the total circular area of the displaced fluid and A_C is the core area of the displacement that is not covered by the inward fingers. For a circular non-fingering displacement d_α equals unity, whereas in the presence of fingering, d_α takes values between zero and unity. As an example, both r_C and r_T are marked in Fig. 2(a). This evaluation is performed at a set radius for all experiments (for $r_T \approx 2.5$ cm), this stage is reached for different times depending on Pe.

In Fig. 5(a), we observe that the instability zone covers a larger area for higher Pe numbers: the d_α ratio decreases while Pe increases, which means that the finger-covered area of the displacement increases with Pe for the same total coverage ($r_T = 2.5$ cm). For the higher Ra number, d_α is higher at comparable

Pe and again decreases with increasing Pe, which means that both quantities have an effect on the VF instability magnitude. Higher radial flow velocities (higher Pe) mean higher driving force for the VF instability and more pronounced pattern formation. With increasing Ra the patterns shift towards the "fan" and the "volcano" regimes in the flow map (Fig. 3), thus VF effects are reduced.

In Fig. 5(b), the dependence of d_α on r_T is depicted for three experiments. For every case, the finger-covered zone is steadily decreasing, *i.e.* d_α is increasing, as the displacement progresses. This is attributed to the radial velocity decay which causes advection to slowly be dominated by diffusive or buoyant effects. Moreover the fingers gradually heal due to diffusive mass transfer and additional coacervate formation. It is again observed that for the same Ra number cases (Ra = 876), the displacement with a higher Pe = 106 099 has a lower d_α, that means more intense fingering instability compared to the Pe = 3979 case.

Depending on the value of Pe, a given spatial location r_T is reached at different times. This could affect the spatio-temporal characteristics of the displacement, both regarding the transport phenomena and the coacervation kinetics since, the lower Pe is, the more physical time elapses until the displacement reaches this r_T point. To investigate this effect, the d_α ratio is also plotted against time for the different displacement experiments in Fig. 5(c). Here, the curves approximately coincide to a uniform progression. This could be due to the fact that the viscous fingers gradually degrade with sufficient time due to the transport effects and the properties of the membrane. Because of the strong velocity decay in the radial geometry, this point is reached at about 400 s for all experimental conditions shown in Fig. 5(c). The limited geometry for higher Pe cases, of course, makes it impossible to evaluate the instability at an equivalent stage. This could obscure phenomena that would occur at later times.

4 Conclusions

To sum up, our experimental study reveals a novel chemically-driven hydrodynamic instability in fluid displacements,
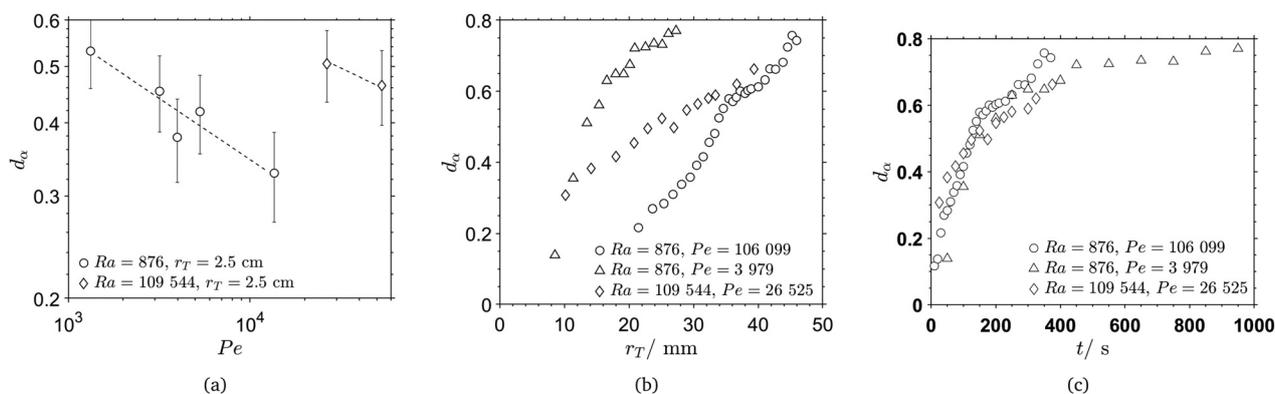

Fig. 5 Analysis of fingering characteristics: (a) dependence of d_α on Pe for two different gap heights, h, corresponding to Ra = 876 and 109 544, (b) progression of d_α with r_T for three different displacement cases, and (c) progression of d_α with t. Lower d_α values correspond to more intense fingering according to eqn (1). The dotted lines in (a) serve as a guide to the eye. The error bars represent the standard deviation among repetition measurements (which was below 10%).

2924 | *Phys. Chem. Chem. Phys.*, 2025, **27**, 2920–2926

This journal is © the Owner Societies 2025

triggered by a coacervation process between a XG dispersion and a $C_{14}TAB$ solution. We showed that the coacervate formed in the contact zone between the two solutions as a weak gel is able to destabilize the displacement which results in pattern formation. Three regimes of instability were identified according to the prevailing driving force: a viscous finger-like pattern, a "fan" pattern governed by the membrane dynamics and a gravity-current dominated "volcano" pattern.

With our classification of the observed displacement regimes in the Ra and Pe parameter space, we condensed the most important influencing parameters in an overview map. The present system shares analogies with similar reaction-diffusion-advection processes, while at the same time it combines aspects of interfacial phenomena, non-Newtonian rheology and buoyancy-induced convection. A major question open for future research is the rheology of the coacervate phase under the different flow conditions, and its coupling to reactant mass transfer effects. In situ micro-rheological studies in combination with numerical simulations of reactive visco-elastic displacements might unravel the complex interactions in this system. The time scale of membrane formation compared to the time scale of mass transfer is a further important aspect, as this ratio changes due to the varying injection rate and also due to the presence or absence of density-driven convection. This is currently only implicitly included in the parameter space of Ra and Pe. Therefore, the Damköhler number can be another important dimensionless number that helps to comprehensively characterize the pattern formation in our system. This requires more detailed studies to estimate the reaction time scale, which is determined by the gradual formation of polymer–surfactant and polymer–micelle complexes and the phase separation by coacervation, leading to membrane formation.

Our experiments form a first basis to select suitable flow parameter ranges providing a desired product distribution and coacervate properties for technological applications. For a given geometry, the system may be tuned to achieve e.g. localized membranes for soil barrier layers or encapsulation, or more widely spread fingering product distributions for remediation or immobilization purposes.

Conflicts of interest

There are no conflicts to declare.

Acknowledgements

Notes and references

1 C. E. Sing and S. L. Perry, Soft Matter, 2020, 16, 2885–2914.

2 I. Mukherjee, D. Sarkar and S. P. Moulik, Langmuir, 2010, 26, 17906–17912.

3 L. Zhou, H. Shi, Z. Li and C. He, Macromol. Rapid Commun., 2020, 41, 2000149.

4 B. Keshavarzi, A. Javadi and A. Bahramian, Pat., WO2019123433, PCT/IB2018/060554, 2018.

5 B. Keshavarzi, K. Schwarzenberger, M. Huang, A. Javadi and K. Eckert, Langmuir, 2019, 35, 13624–13635.

6 K. J. Edler, Soft Matter, 2006, 2, 284–292.

7 A. F. Mason, B. C. Buddingh', D. S. Williams and J. C. M. van Hest, J. Am. Chem. Soc., 2017, 139, 17309–17312.

8 I. G. Veiga and A. M. Moraes, J. Appl. Polym. Sci., 2012, 124, E154–E160.

9 A. Dzionek, D. Wojcieszyńska and U. Guzik, Bioresour. Technol., 2022, 351, 126918.

10 M. H. Abu Elella, E. S. Goda, M. A. Gab-Allah, S. E. Hong, B. Pandit, S. Lee, H. Gamal, A. ur Rehman and K. R. Yoon, J. Environ. Chem. Eng., 2021, 9, 104702.

11 P. G. Saffman and G. I. Taylor, Proc. R. Soc. London, Ser. A, 1958, 245, 312–329.

12 A. De Wit, Annu. Rev. Fluid Mech., 2020, 52, 531–555.

13 L. A. Riolfo, Y. Nagatsu, S. Iwata, R. Maes, P. M. J. Trevelyan and A. De Wit, Phys. Rev. E: Stat., Nonlinear, Soft Matter Phys., 2012, 85, 015304.

14 S. H. Hejazi, P. M. J. Trevelyan, J. Azaiez and A. De Wit, J. Fluid Mech., 2010, 652, 501–528.

15 Y. Nagatsu, Curr. Phys. Chem., 2015, 5, 52–63.

16 S. Berg and H. Ott, Int. J. Greenhouse Gas Control, 2012, 11, 188–203.

17 R. V. Craster and O. K. Matar, Rev. Mod. Phys., 2009, 81, 1131–1198.

18 D.-W. Chung, P. R. Shearing, N. P. Brandon, S. J. Harris and R. E. García, J. Electrochem. Soc., 2014, 161, A422.

19 T. B. Reynolds and G. R. Fink, Science, 2001, 291, 878–881.

20 Y. Nagatsu, Y. Ishii, Y. Tada and A. De Wit, Phys. Rev. Lett., 2014, 113, 024502.

21 F. Haudin and A. De Wit, Phys. Fluids, 2015, 27, 113101.

22 P. Shukla and A. De Wit, Phys. Rev. E, 2016, 93, 023103.

23 D. M. Escala, A. De Wit, J. Carballido-Landeira and A. P. Muñuzuri, Langmuir, 2019, 35, 4182–4188.

24 D. M. Escala and A. P. Muñuzuri, Sci. Rep., 2021, 11, 24368.

25 T. Podgorski, M. C. Sostarecz, S. Zorman and A. Belmonte, Phys. Rev. E: Stat., Nonlinear, Soft Matter Phys., 2007, 76, 016202.

26 Y. Nagatsu, A. Hayashi, M. Ban, Y. Kato and Y. Tada, Phys. Rev. E: Stat., Nonlinear, Soft Matter Phys., 2008, 78, 026307.

27 T. Divoux, A. Shukla, B. Marsit, Y. Kaloga and I. Bischofberger, Phys. Rev. Lett., 2020, 124, 248006.

28 R. X. Suzuki, Y. Nagatsu, M. Mishra and T. Ban, J. Fluid Mech., 2020, 898, A11.

29 R. X. Suzuki, H. Tada, S. Hirano, T. Ban, M. Mishra, R. Takeda and Y. Nagatsu, Phys. Chem. Chem. Phys., 2021, 23, 10926–10935.

30 R. X. Suzuki, Y. Nagatsu, M. Mishra and T. Ban, Phys. Rev. Fluids, 2019, 4, 104005.

31 E. Lemaire, P. Levitz, G. Daccord and H. Van Damme, Phys. Rev. Lett., 1991, 67, 2009–2012.

This journal is © the Owner Societies 2025

Phys. Chem. Chem. Phys., 2025, 27, 2920–2926 | 2925

32 T. A. Camesano and K. J. Wilkinson, *Biomacromolecules*, 2001, **2**, 1184–1191.

33 J. G. Southwick, M. E. McDonnell, A. M. Jamieson and J. Blackwell, *Macromolecules*, 1979, **12**, 305–311.

34 B. Keshavarzi, G. Reising, M. Mahmoudvand, K. Koynov, H.-J. Butt, A. Javadi, K. Schwarzenberger, S. Heitkam, M. Dolgos and A. Kantzas, *et al.*, *Langmuir*, 2024, **40**, 9934–9944.

35 F. Garcia-Ochoa, V. E. Santos, J. A. Casas and E. Gomez, *Biotechnol. Adv.*, 2000, **18**, 549–579.

36 Y. Wang, K. Kimura, P. L. Dubin and W. Jaeger, *Macromolecules*, 2000, **33**, 3324–3331.

37 N. B. Wyatt and M. W. Liberatore, *J. Appl. Polym. Sci.*, 2009, **114**, 4076–4084.

38 P. Petitjeans, C.-Y. Chen, E. Meiburg and T. Maxworthy, *Phys. Fluids*, 1999, **11**, 1705–1716.

39 R. Dorshow, J. Briggs, C. A. Bunton and D. F. Nicoli, *J. Phys. Chem.*, 1982, **86**, 2388–2395.

40 R. Varoqui and A. Schmitt, *Biopolymers*, 1972, **11**, 1119–1136.

41 L. Kondic, M. J. Shelley and P. Palffy-Muhoray, *Phys. Rev. Lett.*, 1998, **80**, 1433–1436.

42 A. Lindner, P. Coussot and D. Bonn, *Phys. Rev. Lett.*, 2000, **85**, 314–317.

43 D. Mokbel and S. Aland, *PAMM*, 2019, vol. 19, p. e201900251.

44 N. Puff, G. Debrégeas, J.-M. di Meglio, D. Higgins, D. Bonn and C. Wagner, *Europhys. Lett.*, 2002, **58**, 524.

45 F. Haudin, L. A. Riolfo, B. Knaepen, G. Homsy and A. De Wit, *Phys. Fluids*, 2014, **26**, 044102.

46 Y. Stergiou, M. J. Hauser, A. De Wit, G. Schuszter, D. Horváth, K. Eckert and K. Schwarzenberger, *Phys. Rev. Fluids*, 2022, **7**, 110503.

47 Y. Stergiou, P. Papp, D. Horváth, Á. Tóth, K. Eckert and K. Schwarzenberger, *Phys. Fluids*, 2023, **35**, 064112.

48 S. Wagatsuma, T. Higashi, Y. Sumino and A. Achiwa, *Phys. Rev. E*, 2017, **95**, 052220.

49 J. Fink and R. Griffiths, *J. Fluid Mech.*, 1990, **221**, 485–509.

50 I. Ziemecka, F. Brau and A. De Wit, *Chaos*, 2020, **30**, 013140.

2926 | *Phys. Chem. Chem. Phys.*, 2025, **27**, 2920–2926

This journal is © the Owner Societies 2025